

A 56-GHz Fractional- N PLL With 110-fs Jitter

Yu Zhao¹, Member, IEEE, Onur Memiöglu, Member, IEEE, Long Kong², Member, IEEE,
and Behzad Razavi³, Fellow, IEEE

Abstract—A fractional- N phase-locked loop (PLL) architecture incorporates a switched-current finite impulse response (FIR) filter to suppress the $\Delta\Sigma$ modulator ($\Delta\Sigma M$) noise. Using a compact, low-power divide-by-8 circuit and realized in 28-nm CMOS technology, the PLL exhibits a phase noise of -98 dBc/Hz at 1-MHz offset in the fractional- N mode while consuming 23 mW and occupying an active area of 0.1 mm².

Index Terms— $\Delta\Sigma$ noise, fractional- N synthesis, master-slave sampling filter, noise folding, non-linearity, phase-locked loop (PLL).

I. INTRODUCTION

THE problem of clock generation with low jitter becomes more challenging as communication systems target higher performance. For example, PAM4 transmitters operating at 112 Gb/s or 224 Gb/s can incorporate a 56-GHz phase-locked loop (PLL) for multiplexing. Such an application poses three conditions on the design. First, the PLL jitter must remain far below the symbol period, e.g., about 100 fs, for a data rate of 224 Gb/s. Second, the PLL should preferably be realized as a fractional- N loop so as to operate with different crystal frequencies and possibly correct for crystal inaccuracies. Third, multi-lane systems make it desirable to use a low-power, compact PLL design per lane rather than distribute a 56-GHz clock across lanes and over long interconnects.

Prior fractional- N designs in this frequency range have achieved rms jitters ranging from 200 to 500 fs while consuming between 31 and 46 mW and requiring chip areas from 0.38 to 0.55 mm² [1], [2], [3].

This article proposes a fractional- N PLL architecture and a number of circuit techniques that achieve an rms jitter of 110 fs with a power of 23 mW. Fabricated in 28-nm CMOS technology, the experimental prototype occupies an active area of 0.1 mm².

Section II provides the background for this work. Section III introduces the proposed finite impulse response (FIR) filter and

Manuscript received 1 May 2022; revised 17 August 2022 and 22 October 2022; accepted 27 October 2022. Date of publication 21 November 2022; date of current version 28 December 2022. This article was approved by Associate Editor Masum Hossain. This work was supported by Realtek Semiconductor. (Corresponding author: Yu Zhao.)

Yu Zhao was with the Department of Electrical and Computer Engineering, University of California at Los Angeles, Los Angeles, CA 90095 USA. He is now with HiSilicon, Shanghai 201206, China (e-mail: zhaoyu@ucla.edu).

Onur Memiöglu is with Apple Inc., Irvine, CA 92618 USA.

Long Kong is with Apple Inc., Cupertino, CA 95014 USA.

Behzad Razavi is with the Department of Electrical and Computer Engineering, University of California at Los Angeles, Los Angeles, CA 90095 USA (e-mail: razavi@ee.ucla.edu).

Color versions of one or more figures in this article are available at <https://doi.org/10.1109/JSSC.2022.3220547>.

Digital Object Identifier 10.1109/JSSC.2022.3220547

0018-9200 © 2022 IEEE. Personal use is permitted, but republication/redistribution requires IEEE permission.
See <https://www.ieee.org/publications/rights/index.html> for more information.

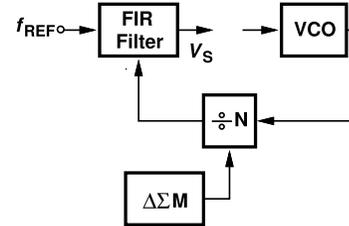


Fig. 1. FIR filtering techniques.

its properties and Section IV describes the PLL architecture. Sections V–VIII deal with the design of the building blocks, and Section VIII presents the experimental results.

II. BACKGROUND

A. PLL Trade-Offs

Fractional- N PLLs face a trade-off among three noise components: 1) the voltage-controlled oscillator (VCO) phase noise; 2) the $\Delta\Sigma$ modulator ($\Delta\Sigma M$) quantization noise (q-noise); and 3) the reference phase noise. As the loop bandwidth (BW) decreases, so do the second and third contributions but at the cost of raising the first. For output jitter values around 100 fs_{rms}, the reference phase noise is negligible if the BW is less than 10 MHz, making the trade-off between the first two the prominent issue. This motivates us to reduce the $\Delta\Sigma$ q-noise by additional methods.

Numerous techniques have been developed to address this point [4], [5], [6], [7], [8], [9], [10], [11], [12]. For example, a digital-to-time converter (DTC) can produce in the reference path phase jumps equal to those created by the feedback divider, thereby presenting a nominally constant error to the phase detector (PD) [4], [9], [12]. This approach, however, requires DTC gain calibration and, more importantly, assumes that the DTC integral nonlinearity is small enough to negligibly fold down the high-pass $\Delta\Sigma$ noise. This in turn demands tight matching among the DTC unit delays.

B. Use of FIR Filters

Another method filters the $\Delta\Sigma$ noise before it reaches the VCO. In [13], for example, an FIR filter is placed after the feedback divider so that delayed copies of the divider output are combined with proper weighting (see Fig. 1). As shown in Fig. 2(a), the divider output phase jumps due to $\Delta\Sigma$ modulation can be viewed as discrete-time samples of a function. If properly delayed, scaled, and summed, these samples yield a much “quieter” output. For the FIR filter to provide attenuation beyond, say, $f_{\text{REF}}/10$, its unit delay must be comparable to T_{REF} , a condition afforded by a chain of

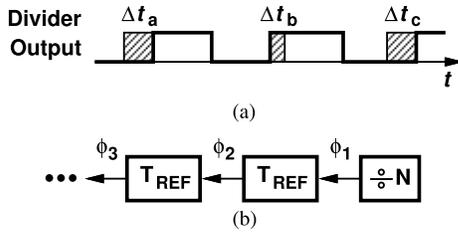


Fig. 2. (a) Output of a divider driven by a $\Delta\Sigma$ M. (b) Delay elements in the FIR filter.

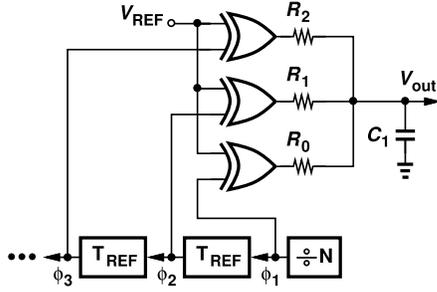


Fig. 3. FIR scaling and summation.

flipflops (FFs) [see Fig. 2(b)] [13]. Since all of the FFs in the delay line are clocked by the prescaler output (at 7 GHz), the excess delay introduced by the FIR filter is less than 50 ps, negligibly affecting the loop stability [13].

This scheme creates delayed copies of the divider output at ϕ_2 , ϕ_3 , etc., but scaling and summing *phase* quantities is not straightforward. For this reason, one can first find the phase difference between these signals and the reference, represent the differences in the voltage domain, and then perform scaling and summation (see Fig. 3) [13]. The resulting feedback signal, V_{out} , exhibits much less fluctuation and drives both the loop filter and the VCO. It is demonstrated in [13] that the loop BW can reach $f_{REF}/4$ with negligible $\Delta\Sigma$ noise contribution.

Although attractive, the foregoing approach does suffer from some nonlinearity as it generates a voltage for the VCO. This point is illustrated in Fig. 4, where two XOR gates form a section of the FIR filter, and the output summation is performed by R_1 , R_2 , and C_1 [13]. Feedback signal ϕ_2 is a delayed copy of the divider output, ϕ_1 . We note that ϕ_1 experiences phase fluctuations Δt_a , Δt_b , etc., due to $\Delta\Sigma$ modulation, and ϕ_2 reproduces these jumps after one reference period, T_{REF} . The output switch samples V_{out} under the command of the reference, V_{REF} . We show that the output samples at V_S have a nonlinear dependence on the phase fluctuations.

Suppose C_1 in Fig. 4 is initially charged to V_{DD} . At $t = t_1$, ϕ_2 rises and C_1 begins to discharge through R_2 . At $t = t_2$, ϕ_1 goes high, causing C_1 to discharge further. With the aid of superposition for V_1 and V_2 , we obtain the sampled output as

$$V_S(t_S) = V_{out}(t_S) = V_{DD} \left[\frac{R_1}{R_1 + R_2} \exp\left(-\frac{(t_S - \Delta t_a)}{\tau}\right) + \frac{R_2}{R_1 + R_2} \exp\left(-\frac{(t_S - \Delta t_b)}{\tau}\right) \right] \quad (1)$$

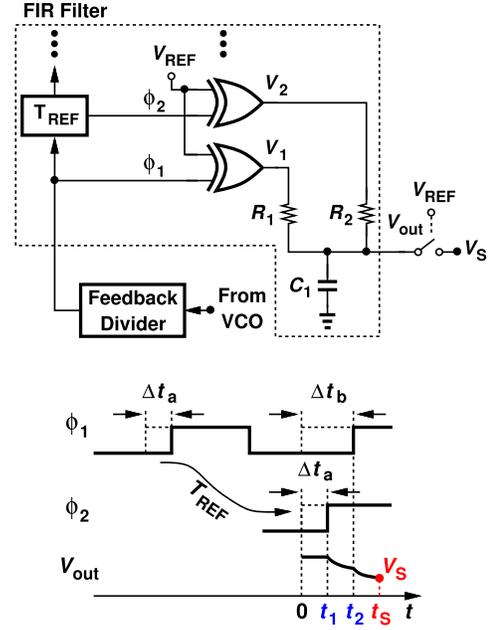


Fig. 4. Resistor-based two-tap FIR filter.

where $\tau = R_1 R_2 C_1 / (R_1 + R_2)$. If $\tau \gg t_S - t_a$ and $t_S - t_b$, then

$$V_S(t_S) \approx V_{DD} \left(1 - \frac{t_S}{\tau} + \frac{\Delta t_a}{R_2 C_1} + \frac{\Delta t_b}{R_1 C_1} \right) \quad (2)$$

revealing that Δt_a and Δt_b are scaled and linearly combined—as expected of an FIR filter. This becomes clearer if we view Δt_b (the divider output phase) as a function, $x(t)$ and note that Δt_a is equivalent to $x(t - T_{REF})$. In practice, however, τ cannot be arbitrarily large because it would lead to low phase detection gain and hence high phase noise contribution from the FIR filter and the following stages.

The key observation here is that the exponential action in (1) makes V_S a nonlinear function of phase jumps Δt_a , Δt_b , etc. Arising *before* the output summation occurs, this phenomenon folds high-pass $\Delta\Sigma$ noise to the baseband. We remark that the nonlinearity originates from two effects. First, the charge delivered to C_1 is nonlinear with respect to the phase jumps because the current flowing through the resistors changes with the output voltage. Second, the branches are never “tristated,” i.e., each resistor charges or discharges C_1 at all times. The significance of these two points becomes clearer in Section III.

It can be shown that a K -tap FIR filter produces a sampled output equal to

$$V_S(t_S) = V_{DD} \sum_{k=1}^K \frac{R_{||}}{R_k} \exp\left(-\frac{(t_S - \Delta t_k)}{\tau}\right) \quad (3)$$

where $R_{||} = R_1 || R_2 || \dots || R_K$ and $\tau = R_{||} C_1$. Moreover, the approximation leading to (2) can be applied here as well to obtain

$$V_S(t_S) \approx V_{DD} \left(1 - \frac{t_S}{\tau} + \sum_{k=1}^K \frac{\Delta t_k}{R_k C_1} \right). \quad (4)$$

Fig. 5 plots the simulated output phase noise of a PLL employing such an FIR filter with $K = 22$ and a third-order $\Delta\Sigma$ M. All other blocks are noiseless. We observe that

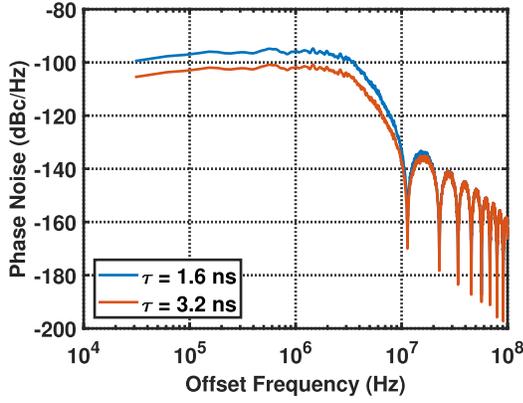


Fig. 5. Simulated $\Delta\Sigma$ M phase noise with a 22-tap resistor-based FIR filter ($f_{\text{REF}} = 250$ MHz, $f_{\text{out}} = 7$ GHz).

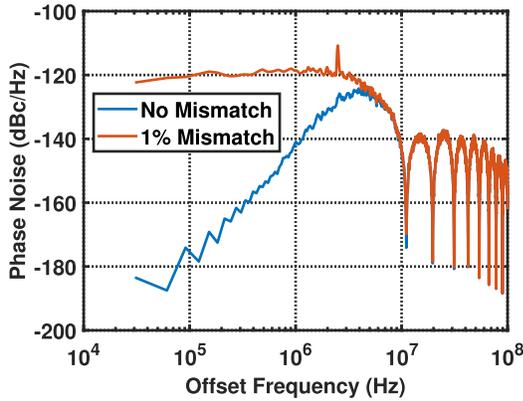


Fig. 6. Simulated $\Delta\Sigma$ M phase noise with a 22-tap CP-based FIR filter ($f_{\text{REF}} = 250$ MHz, $f_{\text{out}} = 7$ GHz).

doubling τ lowers the plateau by 6 dB and the integrated jitter from 920 to 460 fs_{rms} . This can be predicted by writing the Taylor series for the exponential terms in (3).

An important advantage of the proposed FIR filter over charge-pump (CP) PLLs is that it avoids q-noise folding due to the up/down current mismatch. Such a mismatch manifests itself even in multi-input CPs acting as an FIR filter [14], [15]. The CP up/down current mismatch introduces nonlinearity and q-noise folding [16] because the magnitude of the output current depends on the input phase error. According to simulations, a 22-tap CP-based loop with 1% mismatch suffers from considerable folding (see Fig. 6), exhibiting a rise in the integrated jitter from 4 to 81 fs_{rms} . Another advantage of the proposed approach is that it obviates the need for multiple feedback dividers.

III. PROPOSED FIR FILTER

A. Basic Idea

We propose a “switched-current” FIR topology that considerably reduces the nonlinearity described above. We begin with the two-tap structure shown in Fig. 7, where nominally equal current sources I_1 and I_2 are controlled by ϕ_1 and ϕ_2 , respectively. Also depicted are the ϕ_1 and ϕ_2 waveforms along with the output. Assuming V_{out} begins at zero and the current

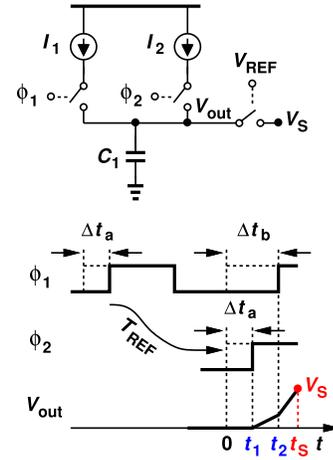


Fig. 7. Switched-current two-tap FIR filter.

sources are ideal, we observe that

$$V_{\text{out}}(t) = -\frac{I_1}{C_1} \Delta t_b - \frac{I_2}{C_1} \Delta t_a + \frac{I_1 + I_2}{C_1} t. \quad (5)$$

In analogy with (1), we recognize a two-tap FIR filter response here, with coefficients $\alpha_1 = -I_1/(I_1 + I_2)$ and $\alpha_2 = -I_2/(I_1 + I_2)$. Note that V_{out} is sampled by V_{REF} so as to perform phase comparison.

The remarkable result here is that $V_{\text{out}}(t)$ in (5) is a linear function of Δt_a and Δt_b , thereby minimizing noise folding. The linearity is obtained fundamentally because the current sources are tristated and have a relatively high output impedance, thus allowing C_1 to store an amount of charge representing the phase difference between the reference and each feedback clock. By contrast, the resistive circuit of Fig. 4 continuously perturbs the output. Using the notation introduced in Section II, we write

$$V_S = \frac{I_1 + I_2}{C_1} [\alpha_1 x(t) + \alpha_2 x(t - T_{\text{REF}}) + t_S]. \quad (6)$$

Departures of α_1 and α_2 from their nominal values slightly alters the FIR transfer function but does not cause nonlinearity. For a K -tap realization, we have

$$V_S(t_S) = \frac{1}{C_1} \sum_{j=1}^K I_j \sum_{j=1}^K \alpha_j (t_S - \Delta t_j) \quad (7)$$

where $\alpha_j = I_j / \sum_{m=1}^K I_m$.

The design of the proposed switched-current FIR filter must deal with a number of questions: 1) how should N and the FIR response be chosen? 2) how should the total current and C_1 be chosen? 3) how does the finite output impedance of the current sources affect the performance? 4) how much is the tolerable noise of the current sources? and 5) how much is the tolerable mismatch among the current sources? We address these questions in Sections III-B and V.

B. FIR Filter Implementation

The FIR filter is realized as shown in Fig. 8(a), where the feedback divider output, ϕ_1 , is delayed by a chain to produce ϕ_2, \dots, ϕ_{22} .

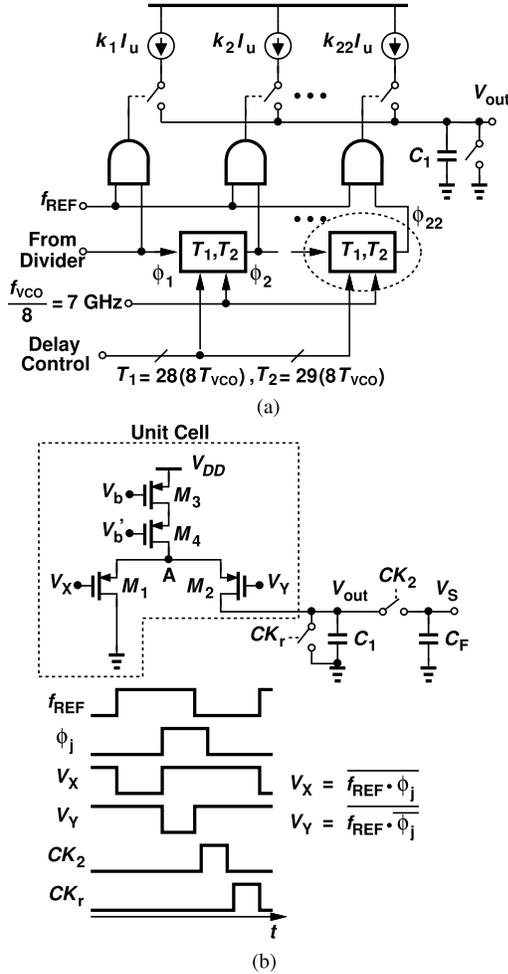


Fig. 8. (a) Implementation of the 22-tap FIR/PD. (b) Unit cell and waveforms of the FIR control signal.

To extract the phase information from these signals, we perform AND functions with the reference. Thus, the pulse widths at the AND gate outputs are equal to the phase differences. Current source j then converts its input pulsewidth to charge, establishing the necessary FIR coefficient, k_j , and C_1 sums the results. This capacitor begins with a zero initial condition so as to avoid intersample interference.

With the proper choice of k_j , the arrangement shown in Fig. 8(a) subjects the divider phase jumps to a low-pass response. It also performs phase comparisons with the reference. We thus expect V_{out} to contain little q-noise.

The unit delays in Fig. 8(a) merit two remarks. First, they are clocked by $f_{VCO}/8 = 7$ GHz, where f_{VCO} denotes the VCO frequency. This choice is justified in Section IV-B. Second, their delay value is selected according to the $\Delta\Sigma$ fractional code word (FCW) to be either $T_1 = 28 \times (8T_{VCO})$ or $T_2 = 29 \times (8T_{VCO})$, where $T_{VCO} = 1/f_{VCO}$. The reason for this “binary delay” is explained in Section VI.

Fig. 8(b) depicts the unit current source implementation. The cascode structure employs a timing scheme that halves the power consumption and yet achieves high linearity. Initially, both M_1 and M_2 are OFF. At the rising edge of f_{REF} , M_1 turns on, bringing V_A down to a desired value. Then, on the rising

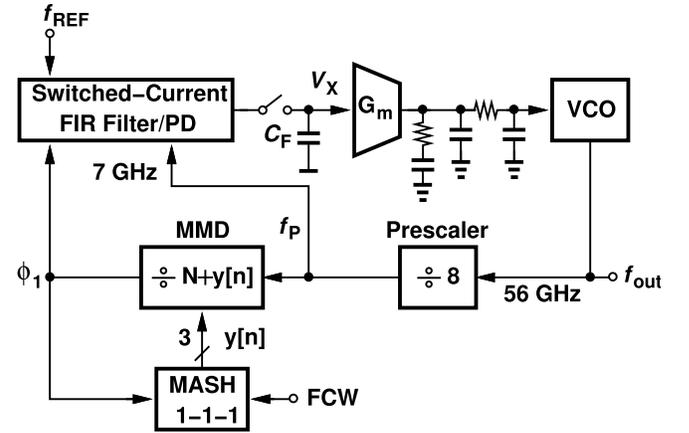


Fig. 9. Proposed PLL architecture.

edge of ϕ_j , M_1 turns off, M_2 turns on, and C_1 begins to charge. In this design, we ensure an overlap of 8 ps between V_Y and V_X so that V_A does not take off toward V_{DD} during this transition.

As shown in Fig. 8(b), the voltage developed across C_1 is applied to another capacitor, C_F , when CK_2 goes high. This action prohibits the transient on C_1 from reaching the VCO and causing jitter. With $C_F \approx 0.25 C_1$, some charge sharing occurs, but it can be shown that this effect does not introduce nonlinearity. After CK_2 falls, CK_r reset C_1 .

IV. PROPOSED PLL ARCHITECTURE

The proposed fractional- N PLL architecture is shown in Fig. 9. A LC VCO is followed by a low-power, compact $\div 8$ circuit acting as a prescaler and a multimodulus divider (MMD). The MMD output travels through a switched-current FIR filter, a PD, and a sampler, returning a voltage to a Gm stage, which drives the loop filter. The FFs comprising the FIR delay units are clocked by the $\div 8$ circuit output. The third-order $\Delta\Sigma M$ is realized by a MASH 1-1-1 topology. With a word length of 20 bits, this modulator provides a frequency resolution of 2 kHz at 56 GHz, i.e., about 0.04 ppm. This is well below typical crystal frequency tolerances.

A. Design Considerations

The proposed architecture entails a number of considerations. First, since an MMD operating at 56 GHz would consume substantial power and require inductive peaking, we lower the clock frequency before applying it to the MMD. The trade-offs in this choice are quantified in Section IV-B.

Second, despite the limited speed of the 28-nm CMOS devices, the PLL incorporates only one inductor (in the VCO) so as to occupy a small footprint. This is made possible by a new $\div 2$ circuit topology used in the prescaler (see Section VII-A). Third, the output of the FIR filter is sampled on capacitor C_F before it is reset to zero according to Fig. 8(a). Fourth, the Gm stage in Fig. 9 exhibits a low-frequency voltage gain of 30 dB, thus relaxing the voltage compliance at the FIR filter output. This greatly relaxes the design of the unit current sources, but the noise of the Gm circuit must be managed. Fifth, the loop BW is chosen equal to 4 MHz so as to minimize

the total integrated phase noise due to the VCO and the FIR-filtered contribution of the $\Delta\Sigma$. Sixth, to save power, the VCO and divider chain employ no buffer. Thus, the VCO must absorb the input capacitance of the prescaler.

The PLL of Fig. 9 incorporates a sampling PD, generating a voltage, V_X , proportional to the phase error. To compute the PD gain, K_{PD} , we assume integer- N operation and note that the FIR filter current, I_{tot} , flows through C_1 in Fig. 8(a). With a slope of I_{tot}/C_1 , V_X provides a change of $\Delta t I_{tot}/C_1$ for a phase error of Δt seconds. The PD gain in V/rad is thus equal to

$$K_{PD} = \frac{I_{tot}}{2\pi f_{REF} C_1}. \quad (8)$$

The proposed PD can be approximately modeled by the following transfer function [17]:

$$H_{PD}(j\omega) = K_{PD} \cdot \frac{1}{1 + \frac{C_2}{C_1 f_{REF}} j\omega} e^{-j\omega T_{REF}/2} \frac{\sin(\omega T_{REF}/2)}{\omega T_{REF}/2}. \quad (9)$$

B. Choice of Prescaler Modulus

The prescaler divide ratio M in Fig. 9 is preferably equal to a power of 2. A greater value favors the design of the MMD but at the cost of larger phase jumps in ϕ_1 . For example, with $M = 8$ and hence $f_P = 7$ GHz, the maximum phase step in ϕ_1 is equal to ± 286 ps for a MASH 1-1-1 modulator. With $M = 4$, on the other hand, this jump is only ± 143 ps. The PLL output phase noise is the absence of the FIR filter exhibits a bandpass shape and is equal to

$$S_{\Phi_{\Delta\Sigma}} = \frac{4\pi^2 M^2}{12 f_{REF}} \cdot \left(2 \sin \frac{\pi f}{f_{REF}} \right)^4 |G(f)|^2 \quad (10)$$

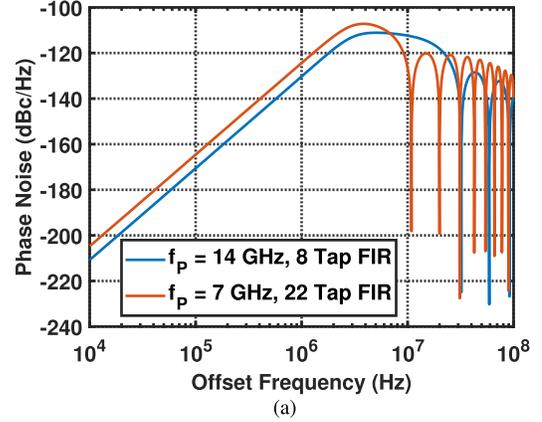
where a MASH 1-1-1 architecture is assumed and $G(f)$ denote the PLL transfer function [18]. To counter the effect of M^2 , the FIR filter length must be *greater* so as to provide a sharper roll-off, translating to a larger number of FFs. The total number of FFs is given by $(K - 1)f_P/f_{REF}$, where K is the number of taps and f_P the prescaler output frequency.

In summary, as M increases: 1) the prescaler draws more power; 2) the MMD draws less; and 3) the FIR filter runs at lower clock frequency but requires a larger number of taps. Since most of the power consumption by the filter occurs in its clock path, we can write

$$P_{FIR} = f_P \frac{(K - 1)f_P}{f_{REF}} C_{FF} V_{DD}^2 \quad (11)$$

where C_{FF} denotes the clock input capacitance of each FF. A higher M yields a lower f_P while demanding a higher K . To determine the optimum M , we assume a certain $\Delta\Sigma$ -induced jitter, e.g., 40 fs_{rms}, and a loop BW of 4 MHz, and quantify these three effects.

Plotted in Fig. 10(a) are the PLL output spectra due to the $\Delta\Sigma$ q-noise for the two cases, both exhibiting an rms jitter of 40 fs. We now use transistor-level simulations to compute the power drawn by the prescaler, the MMD, and the FIR filter, obtaining the values shown in Fig. 10(b). It follows that



	$M = 8$	$M = 4$
P_{pre}	3.1 mW	2.7 mW
P_{FIR}^*	6 mW	8 mW
P_{MMD}	1 mW	1.9 mW
Total	10.1 mW	12.6 mW

* Only the clock path power included

Fig. 10. (a) PLL output $\Delta\Sigma$ phase noise spectra with $\div 4$ and $\div 8$ prescaler. (b) Power breakdown.

$M = 8$ is preferable. While a more aggressive design could consider $M = 16$, it necessitates $K = 56$ for the FIR filter and hence a very large number of FFs.

V. FIR FILTER DESIGN

We have presented the FIR filter topology in Section IV but also have raised a number of questions about its attributes in Section III-A. In this section, we deal with the questions.

A. Filter Response and Length

The frequency response of the filter is determined by the number of its taps, K , and its coefficients, k_1, k_2, \dots, k_K . In this work, we employ a Chebyshev response as it does not require a high resolution for the unit current sources. Specifically, we have $k_1 = k_{22} = 10$ units, $k_2 = k_{21} = 3$ units, \dots , and $k_{11} = k_{12} = 5$ units. The number of taps, $K = 22$, is chosen as a compromise between the filter power consumption and the $\Delta\Sigma$ q-noise suppression.

The efficacy of the proposed FIR architecture can be assessed by several metrics: 1) the $\Delta\Sigma$ q-noise spectrum is reduced by 18 dB at 10 MHz; 2) the integrated $\Delta\Sigma$ noise is suppressed by 12 dB; and 3) the probability density function of the phase error is narrowed from $\pm 2T_{div}$ at the MMD output to (equivalently) $\pm 0.3T_{div}$ at the FIR output (see Fig. 11).

B. Mismatch and Noise of Current Sources

As mentioned in Section III, random mismatches among the current sources in Fig. 8(a) do not introduce nonlinearity but alter the response. In a typical current-source array, PMOS mismatches can be readily maintained below 10%. We thus perform Monte Carlo simulations to determine the variation of the FIR response and hence the PLL output jitter with this amount of mismatch. Plotted in Fig. 12, the tight distribution reveals the robustness of the design.

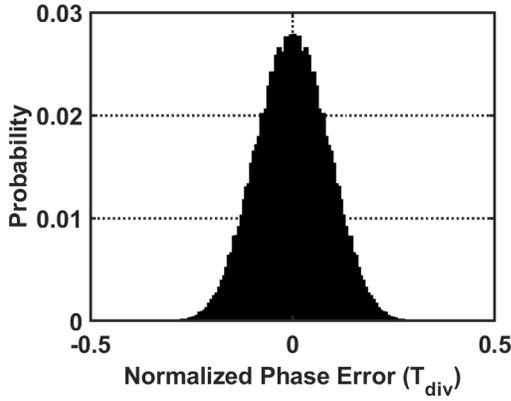
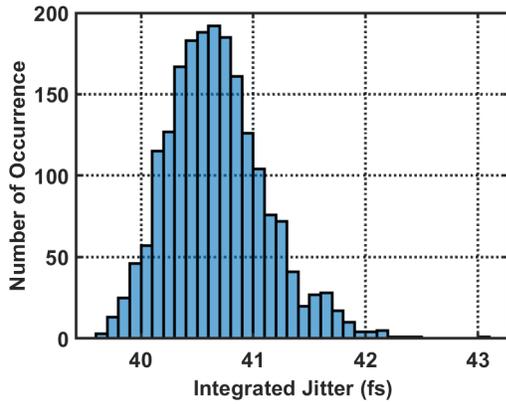
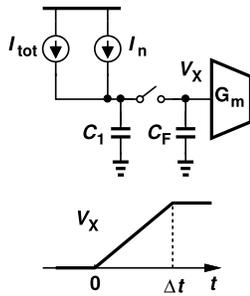
Fig. 11. Histogram of equivalent $\Delta\Sigma$ phase error at the FIR output.Fig. 12. Monte-Carlo results showing variation of $\Delta\Sigma$ M-induced jitter.

Fig. 13. Analysis of FIR output noise.

The noise of current sources in Fig. 8(a) is deposited on C_1 when they are enabled, corrupting the control voltage of the oscillator. For a current of I_D , the thermal noise current spectrum is approximately equal to $8kT\gamma I_D/(V_{GS} - V_{TH})$, dictating a large overdrive voltage and hence a limited output voltage compliance. We must therefore quantify the corruption and ensure that it contributes negligible jitter. To arrive at an approximation, we assume all of the current sources are enabled and seek the noise spectrum appearing on C_F in Fig. 9. Consider the simplified model shown in Fig. 13, where I_{tot} and I_n represent the total current and its noise component, respectively. The integration of I_n for Δt seconds leads to the following noise voltage on C_1 [19]:

$$v_n = \frac{1}{C_1} \int_{-\infty}^{+\infty} i_n(t)w(t)dt \quad (12)$$

where $w(t)$ denotes a square pulse extending from 0 to Δt with a height of unity. This noise is sampled at a rate of f_{REF} , yielding an output spectrum of [19]

$$S_{V_n}(f) = \frac{1}{C_1^2} |W(f)|^2 S_{I_n}(f) \quad (13)$$

where $W(f)$ is the Fourier transform of the square pulse and $S_{I_n}(f)$ the spectrum of I_n . It is also proved in [19] that window-integrated, sampled white noise has a white spectrum if $\Delta t < T_{REF}$. That is

$$S_{V_n}(f) = \frac{1}{(C_1 + C_F)^2} \frac{\Delta t}{f_{REF}} S_{I_n}(f) \quad (14)$$

where the charge sharing between C_1 and C_F is included. Dividing this spectrum by K_{PD}^2 yields the input-referred phase noise arising from the FIR filter

$$S_{\phi, \text{white}} = 4\pi^2 \frac{\Delta t}{T_{REF}} \frac{C_1^2}{(C_1 + C_F)^2} \frac{S_{I_n}(f)}{I_{tot}^2}. \quad (15)$$

In a similar manner, the effect of flicker noise current, $S_{1/f}(f)$, can be formulated as

$$S_{\phi, 1/f} = 4\pi^2 \frac{\Delta t^2}{T_{REF}^2} \frac{C_1^2}{(C_1 + C_F)^2} \frac{S_{1/f}(f)}{I_{tot}^2} \quad (16)$$

where noise aliasing is neglected. As a worst case estimate, we assume the maximum Δt that occurs in the fractional- N mode. For a MASH 1-1-1 modulator, and a prescaler divide ratio of 8, Δt reaches $\pm 16T_{VCO} \approx 280$ ps. We note that doubling I_{tot} and C_1 reduces both thermal noise and flicker noise by 3 dB.¹ With $I_{tot} = 7$ mA, $C_1 = 6$ pF and $C_F = 1.5$ pF,² we obtain an input-referred phase noise of -157 dBc/Hz at 1-MHz offset. This value translates to -110 dBc/Hz at the PLL output. With fractional- N operation, we expect similar results. According to simulations, the output jitter rises by 9 fs when the noise of the FIR current sources is included.

C. Output Resistance of Current Sources

As mentioned in Section III, the proposed switched-current FIR filter relies on two properties to avoid noise folding: tristate action of each branch, and a current provided by each branch that is relatively independent of the output voltage. The latter premise must be reexamined in view of the finite output resistance of the current sources.

Consider the simplified two-tap circuit shown in Fig. 14, where R_1 and R_2 denote the output resistance of I_1 and I_2 , respectively. We repeat the calculations of Section III for this case, obtaining

$$V_{out}(t) = (V_{DD} + I_1 R_1) \cdot \left[1 - \exp\left(\frac{(R_{||}/R_2)\Delta t_a + (R_{||}/R_1)\Delta t_b - t}{R_{||}C_1}\right) \right]. \quad (17)$$

Interestingly, the FIR action (scaling and summation of Δt_a and Δt_b) occurs here *before* nonlinearity takes over.

¹We keep I_{tot}/C_1 to 1.1 GV/s so that Δt is large enough to accommodate the $\Delta\Sigma$ phase error.

²The FIR current sources charges C_1 from zero to 0.5 V in 430 ps. This charging time is less than half of the reference period.

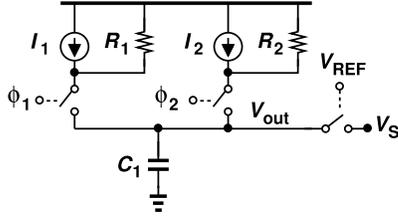
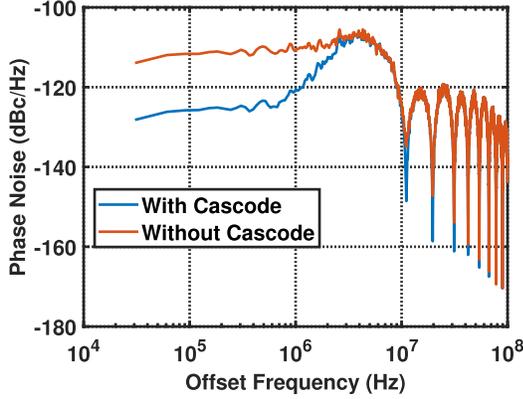
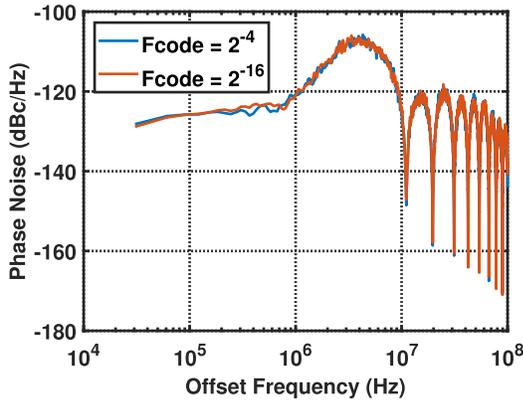


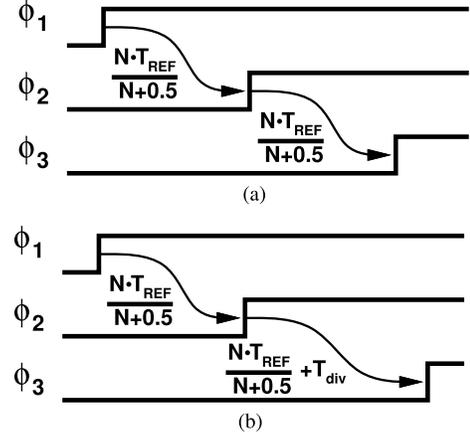
Fig. 14. Two-tap switched-current FIR filter with finite output resistance.


 Fig. 15. PLL output phase noise profiles ($f_{out} = 56$ GHz, $f_P = 7$ GHz).

 Fig. 16. PLL output phase noise profiles for large and small FCWs ($f_{out} = 56$ GHz, $f_P = 7$ GHz).

Thus, if FIR filtering suppresses the high-frequency noise, the exponential introduces negligible folding.

Of course, if we decrease R_1 and R_2 indefinitely, folding becomes significant. This points to the need for the cascode topology in Fig. 8(b). Plotted in Fig. 15 are the PLL output phase noise profiles due to the $\Delta\Sigma$ M for simple and cascode current sources. The latter is close to that shown in Fig. 10(a) for $f_P = 7$ GHz, a 22-Tap FIR, and ideal current sources. Nevertheless, the high output resistance is afforded for only a maximum output voltage of about 600 mV, thereby requiring the voltage gain provided by the Gm stage (see Section IV).

It is possible to improve the linearity of the FIR filter by increasing C_1 so that the exponential in (17) can be approximated by its linear terms. However, this increases Δt in (15) and (16), raising the noise contribution of the current sources.


 Fig. 17. FIR delay output waveform (a) without binary delay and (b) with binary delay. (FCW = $\alpha = 0.5$.)

To appreciate the efficacy of the FIR filter, we simulate the fractional- N PLL without it, obtaining an integrated jitter of 190 fs_{rms}, 70% of which arises from the $\Delta\Sigma$ noise. If the loop filter's BW is reduced by a factor of 2, the overall jitter falls to a minimum of 140 fs_{rms}, still far above our overall target.

According to simulations, the PLL output q-noise floor changes negligibly as we reduce FCW from 2^{-4} to 2^{-16} (see Fig. 16). Thus, the FIR concept proves effective for small FCWs as well.

VI. DELAY LINE DESIGN

The unit delays in the FIR filter of Fig. 8(a) consist of FFs and are clocked with a period of $T_{div} = 8T_{VCO}$. With this clocking method, ϕ_2 - ϕ_{22} carry the feedback information for the PLL to lock [13]. However, since T_{div} and T_{REF} do not bear an integer ratio, the phase difference sensed by the filter accumulates with time, eventually reaching large values [see Fig. 17(a)]. This in turn produces an excessive voltage change on C_1 and causes the current source(s) to collapse. To resolve this issue, the delay elements can assume either of two values, namely, $T_1 = 28T_{div}$ or $T_1 = 29T_{div}$, so as to create a tight bound for this error. Programmed individually in conjunction with the $\Delta\Sigma$ M FCW, α , the delay of Stage j is set according to the following rules. If the accumulated error from Stage 1 to Stage j is less than T_{div} , then $T_1 = 28T_{div}$ is selected. Otherwise, $T_2 = 29T_{div}$. As depicted by the waveform in Fig. 17(b), the delay from ϕ_2 to ϕ_3 is compensated by one more T_{div} , limiting the phase error in the last tap, ϕ_{22} , to about T_{div} .

The FFs employ a true single-phase clock (TSPC) structure (see Fig. 18). The total extracted capacitance of the clock input is 1.2 fF. This work employs 600 FFs, consuming $P = fCV_{DD}^2 = 6$ mW at 7 GHz.

VII. DIVIDER DESIGN

The power and area consumption of dividers can become significant at the frequencies of interest here. For this reason, it is desirable to avoid current-mode logic and inductive peaking. This section deals with both the prescaler and the MMD.

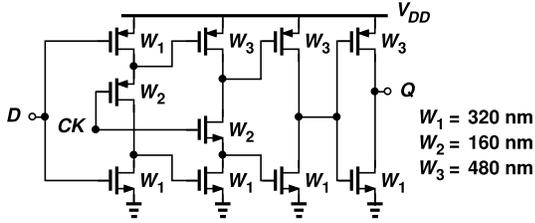
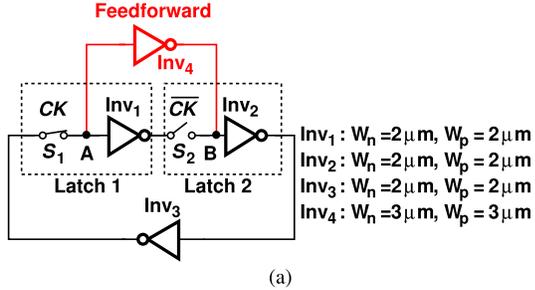


Fig. 18. TSPC FF in the FIR delay element.



Process Corner	Input Freq. (GHz)	
	Min	Max
TT	43.1	68.3
SS	37.1	59.2
FF	52.5	77.5
FS	48.6	70.6
SF	41.2	66.4

(b)

Fig. 19. (a) $\div 2$ circuit with feedforward and (b) its simulated frequency range over process corners.

A. Prescaler

The $\div 8$ circuit consists of three cascaded $\div 2$ stages. The first must present a low capacitance to the VCO while providing sufficiently large voltage swings to drive the second. We propose a low-power, compact topology. As shown in Fig. 19(a), the circuit is based on two dynamic latches and a third inverter in the feedback path for proper toggling.

The performance is dramatically improved by introducing an unlocked feedforward path from A to B so that the signal arrives at the latter before S_2 turns on. This “predictive” path therefore initiates a desirable change in the state at B while S_2 is still OFF. Proper scaling of Inv_4 with respect to those in the main path extends the upper end of the lock range while imposing some limitation on the lower end. That is, at sufficiently low clock frequencies, the feedforward path overwhelms the main path, causing failure.

Switches S_1 and S_2 in Fig. 19(a) are realized by NMOS transistors that are $2 \mu\text{m}$ wide, with their gates residing at a dc level of V_{DD} . As the gate voltages of S_1 and S_2 rise above V_{DD} , their V_{gs} reach 1.28 V, slightly stressing these devices. Using the model described in [20], we compute the estimated lifetime at 0.01% cumulative failure rate to be 11.3 years at 140°C . The capacitively-coupled clocks then allow a low resistance for these devices. Fig. 19(b) shows the simulated input frequency range of the proposed $\div 2$ stage over process corners. The layout parasitics are included. We observe that feedforward raises the maximum speed from 55 to 68 GHz and limits the lower end to 43 GHz. The circuit draws 1.8 mW at 56 GHz and presents an input capacitance of 10 fF to the VCO.

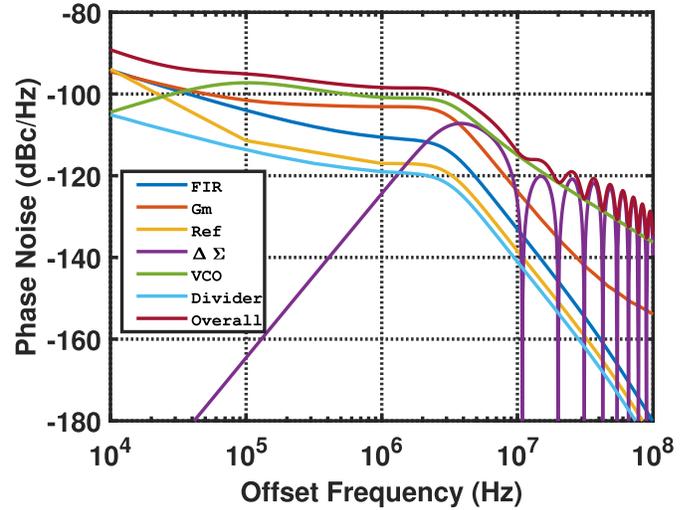


Fig. 20. Simulated PLL output phase noise.

TABLE I
JITTER CONTRIBUTION

Building Block	Jitter Contribution (fs)
Reference	14.2
$\Delta\Sigma$	40
VCO	80.6
FIR	26.1
Gm	55.3
Divider	9.3
Overall	110

B. Multimodulus Divider

The MMD is implemented by a cascade of $\div 2/3$ stages [21] and its modulus can range from 16 to 63. The first two stages are implemented by TSPC logic and the rest by CMOS logic [22]. The MMD draws 1 mW at 7 GHz.

VIII. JITTER CONTRIBUTIONS

Fig. 20 plots the simulated PLL output phase noise components arising from the reference, the $\Delta\Sigma$, the FIR filter, the Gm stage, the VCO, and the feedback divider chain for a loop BW of 4 MHz. According to simulations, the $\Delta\Sigma$ q-noise translates to an rms jitter of 160 fs without the proposed FIR filter.

The VCO is based on a complementary LC topology with $W/L = 15 \mu\text{m}/40 \text{ nm}$ for all four transistors. The 45-pH differential inductor is realized as a parallel stack of metal-9 and metal-8 spirals so as to reduce the resistance. Although this inductor’s Q is about 20 at 56 GHz, the addition of programmable capacitors drops the Q to approximately 13. The VCO achieves a tuning range of 52.3–56.8 GHz with a phase noise of -94 dBc/Hz at 1-MHz offset while consuming 7.2 mW.

Table I summarizes the corresponding jitter contributions, demonstrating the efficacy of the FIR filter in suppressing the $\Delta\Sigma$ q-noise. The VCO and the Gm stage are the principal contributors.

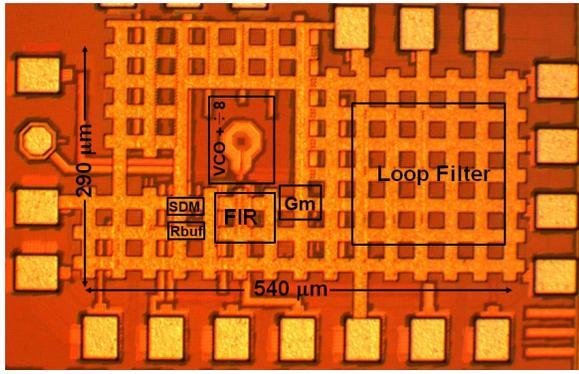


Fig. 21. Die photograph.

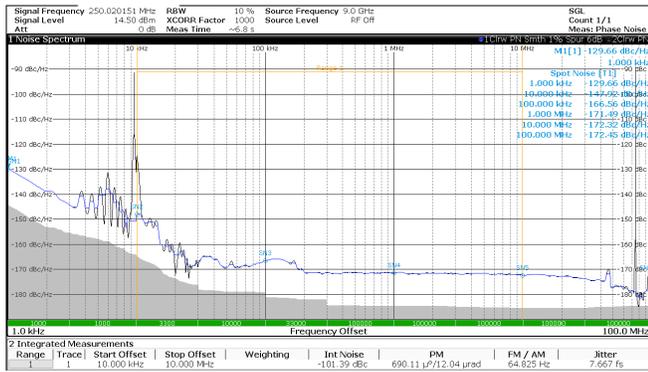


Fig. 22. Measured phase noise of the 250-MHz crystal oscillator.

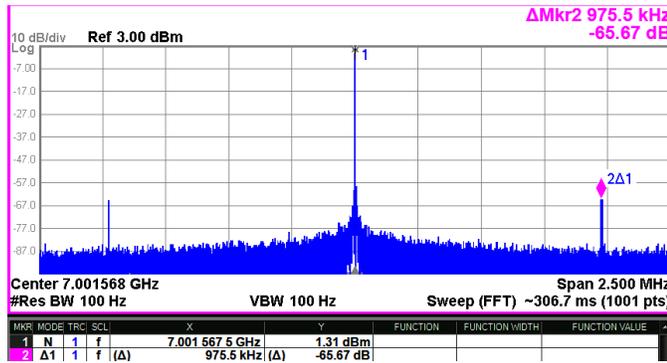


Fig. 23. Measured PLL output spectrum.

IX. EXPERIMENTAL RESULTS

The proposed PLL has been fabricated in TSMC’s 28-nm CMOS technology. Fig. 21 shows a photograph of the die, whose active area measures approximately 0.1 mm^2 .³ Operating with a 1-V supply, the prototype consumes 23 mW. The external 250-MHz reference is supplied by Crystek’s CRBSCS-01-250 250-MHz crystal oscillator.⁴ Its measured phase noise is plotted in Fig. 22. For ease of measurement, the output of the $\div 8$ prescaler in Fig. 9 is monitored for characterization of the PLL.

Fig. 23 shows the measured spectrum at this point with $\text{FCW} = 28.004$. The fractional spur at 1-MHz offset has a level of -65.7 dBc , which translates to -47.7 dBc at the VCO

³The area of the loop filter is dominated by the series capacitor to create a zero at 800 kHz.

⁴The supply voltage of the crystal oscillator is 5.5 V.

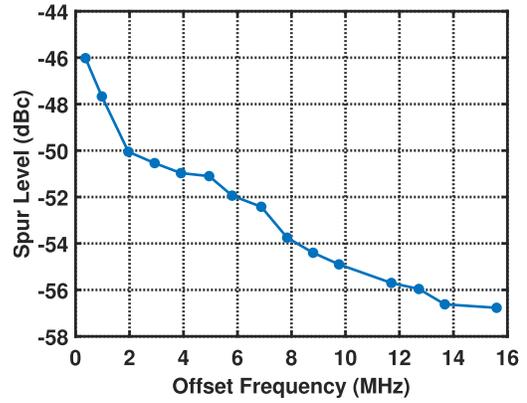
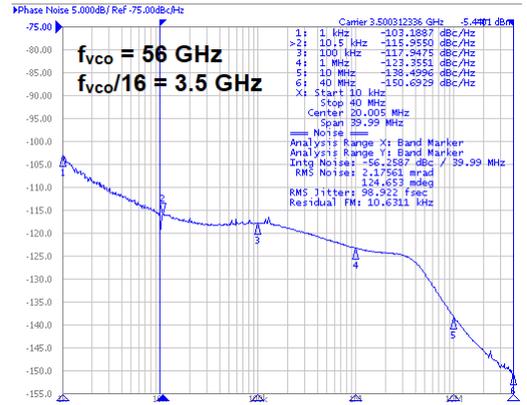
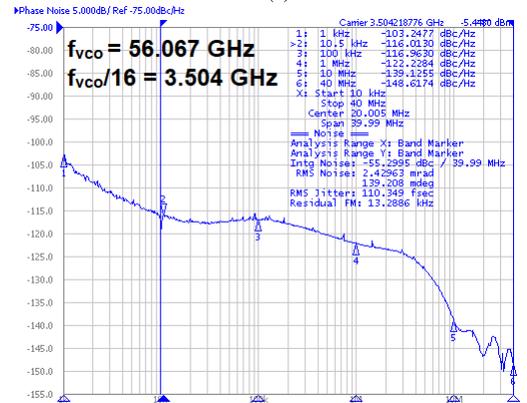


Fig. 24. Measured PLL fractional spur levels.



(a)



(b)

Fig. 25. Measured PLL output phase noise in (a) integer- N mode and (b) fractional- N mode.

output. Fig. 24 plots the fractional spur levels as FCW varies from 28.0015 to 28.06 and hence the fractional spur offset frequency from 0.4 to 15 MHz. We should make two remarks. First, the measured spur levels reported here are about 3 dB lower than those in [23]. This has been achieved by separating the supply lines of the delay line, the Gm stage, and the FIR filter and refabricating the chip. Second, wireline receivers typically allow a BW of tens of megahertz [24], [25] or even above 100 MHz [26], [27] in their clock and data recovery (CDR) loop. As the CDR ensures the recovered clock phase tracks that of the received data, fractional spurs are rejected within the CDR loop BW. For example, a -50-dBc spur at 2-MHz offset negligibly affects the receiver performance even

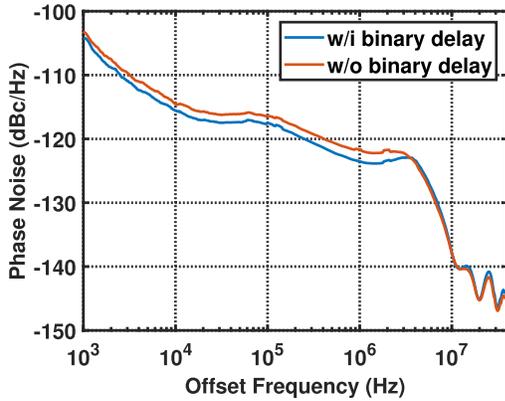


Fig. 26. Measured PLL output phase noise with binary delay line enabled and disabled.

TABLE II
PERFORMANCE SUMMARY AND COMPARISON TO PRIOR ART

	Wu ISSCC 2013	Hussein ISSCC 2017	Grimaldi ISSCC 2014	Zong JSSC 2019	This Work
Freq. Range (GHz)	56.4~63.4	50.2~66.5	30.6~34.2	57.5~67.2	52.3~56.8
RMS Jitter (fs)	522.9	223	197.6	213	110
Integ. range (MHz)	(0.01~10)	(0.001~40)	(0.001~10)	(0.01~30)	(0.01~40)
Normalized PN (dBc/Hz) *	-70.7	-83.3	-82.4	-83.3	-92
Frac. Spur (dBc)	N/A	-68	-42.2	-38	-46
Ref. Spur (dBc)	-74	-N/A	N/A	-65	-50
Ref. Freq. (MHz)	100	100	100	100	250
Tech. (nm)	65	65	65	28	28
Power (mW)	40	46	35	31	23
Supply Voltage (V)	1.2	1	1.2	1.05	1
Bandwidth (MHz)	0.3	0.3~5	0.5	0.2~0.3	4
Active Area (mm ²)	0.48	0.45	0.55	0.38	0.1
FoM ₁ (dB)	-229.6	-236.4	-238.6	-237.2	-245.5
FoM ₂ (dB)	-257.4	-264.2	-263.6	-265.0	-269

$$\text{FoM}_1 = 10 \log_{10} \left[\left(\frac{\text{Jitter}}{1 \text{ s}} \right)^2 \left(\frac{\text{Power}}{1 \text{ mW}} \right) \right] \quad \text{FoM}_2 = 10 \log_{10} \left[\left(\frac{\text{Jitter}}{1 \text{ s}} \right)^2 \left(\frac{\text{Power}}{1 \text{ mW}} \right) \left(\frac{f_{\text{ref}}}{f_{\text{PLL}}} \right) \right]$$

* Phase noise at 100 kHz is normalized to 56 GHz.

though it translates to a deterministic jitter of 12.7 fs_{rms} at the transmitter output.

Due to our phase noise analyzer limitations, the ÷8 output is applied to an off-chip divide-by-2 circuit for phase noise measurements. Fig. 25(a) plots the phase noise for the integer-*N* mode, yielding an rms jitter of 99 fs. Fig. 25(b) shows the measured phase noise in the fractional-*N* mode with FCW = 28.034. The in-band phase noise at 1-MHz offset referred to the VCO output is -98.2 dBc/Hz. The integrated jitter is computed in two different BWs. First, for a fair comparison with the prior art, the offset ranges from 10 kHz to 40 MHz, yielding a total of 110 fs_{rms}. Second, the offset ranges from 40 MHz to the Nyquist frequency of 3.5 GHz, revealing another 31 fs. (Due to the equipment limitation, this measurement reads the phase noise values directly from the spectrum of the ÷8 output.) Thus, the total jitter from 10 kHz to 3.5 GHz is 114 fs_{rms}.

In order to study the advantage of the binary delay line, we set the FCW to 0.127 and measure the PLL phase noise. We first set a single delay value for the entire FIR chain and then enable the binary delay option. Plotted in Fig. 26 are the phase noise profiles for the two cases. Enabling the binary

delay reduces the phase noise by 1 to 1.5 dB below 3-MHz offset and the integrated jitter by 10 fs.

Table II summarizes the measured performance of our prototype and compares it to that of prior-art 60- and 30-GHz fractional-*N* PLLs. We observe a nearly twofold reduction in jitter, an 8.3-dB improvement in the figure of merit (FoM), and more than a threefold reduction in area. We also list FoM₂, proposed in [28], since the reference frequency in our prototype is higher than other PLLs in Table II. The reference spur level is -50 dBc and translates to a deterministic jitter of 12.7 fs_{rms} in the transmitted data.

X. CONCLUSION

This article proposes a new fractional-*N* PLL architecture that suppresses the $\Delta\Sigma$ noise and lends itself to a compact low-power design. A new ÷2 circuit is also described.

REFERENCES

- [1] A. Hussein, S. Vasadi, M. Soliman, and J. Paramesh, "19.3 A 50-to-66 GHz 65 nm CMOS all-digital fractional-*N* PLL with 220fs_{rms} jitter," in *IEEE Int. Solid-State Circuits Conf. (ISSCC) Dig. Tech. Papers*, Feb. 2017, pp. 326–327.
- [2] W. Wu, X. Bai, R. B. Staszewski, and J. R. Long, "A 56.4-to-63.4 GHz spurious-free all-digital fractional-*N* PLL in 65 nm CMOS," in *Proc. IEEE Int. Solid-State Circuits Conf. Dig. Tech. Papers*, Feb. 2013, pp. 352–353.
- [3] Z. Zong, P. Chen, and R. B. Staszewski, "A low-noise fractional-*N* digital frequency synthesizer with implicit frequency tripling for mm-Wave applications," *IEEE J. Solid-State Circuits*, vol. 54, no. 3, pp. 755–767, Mar. 2019.
- [4] D. Tasca et al., "A 2.9–4.0-GHz fractional-*N* digital PLL with bang-bang phase detector and 560-fs_{rms} integrated jitter at 4.5-mW power," *IEEE J. Solid-State Circuits*, vol. 46, no. 12, pp. 2745–2758, Dec. 2011.
- [5] L. Grimaldi et al., "A 30 GHz digital sub-sampling fractional-*N* PLL with 198fs_{rms} jitter in 65 nm LP CMOS," in *IEEE ISSCC Dig. Tech. Papers*, Feb. 2019, pp. 268–270.
- [6] D. Yang et al., "A calibration-free triple-loop bang-bang PLL achieving 131fs_{rms} jitter and -70 dBc fractional spurs," in *IEEE ISSCC Dig. Tech. Papers*, Feb. 2019, pp. 266–268.
- [7] W. Wu et al., "A 14-nm ultra-low jitter fractional-*N* PLL using a DTC range reduction technique and a reconfigurable dual-core VCO," *IEEE J. Solid-State Circuits*, vol. 56, no. 12, pp. 3756–3767, Dec. 2021.
- [8] A. Elkholy, T. Anand, W.-S. Choi, A. Elshazly, and P. K. Hanumolu, "A 3.7 mW low-noise wide-bandwidth 4.5 GHz digital fractional-*N* PLL using time amplifier-based TDC," *IEEE J. Solid-State Circuits*, vol. 50, no. 4, pp. 867–881, Apr. 2015.
- [9] N. Pavlovic and J. Bergervoet, "A 5.3 GHz digital-to-time-converter-based fractional-*N* all-digital PLL," in *IEEE ISSCC Dig. Tech. Papers*, Feb. 2011, pp. 54–56.
- [10] H. Liu et al., "A sub-mW fractional-*N* ADPLL with FOM of -246 dB for IoT applications," *IEEE J. Solid-State Circuits*, vol. 53, no. 12, pp. 3540–3552, Dec. 2018.
- [11] X. Gao et al., "A 28 nm CMOS digital fractional-*N* PLL with -245.5dB FOM and a frequency tripler for 802.11abgn/AC radio," in *IEEE ISSCC Dig. Tech. Papers*, Feb. 2015, pp. 1–3.
- [12] K. Raczkowski, N. Markulic, B. Hershberg, and J. Craninckx, "A 9.2–12.7 GHz wideband fractional-*N* subsampling PLL in 28 nm CMOS with 280 fs RMS jitter," *IEEE J. Solid-State Circuits*, vol. 50, no. 5, pp. 1203–1213, May 2015.
- [13] L. Kong and B. Razavi, "A 2.4-GHz RF fractional-*N* synthesizer with BW=0.25 *f*_{REF}," *IEEE J. Solid-State Circuits*, vol. 53, no. 6, pp. 1707–1718, Feb. 2018.
- [14] X. Yu et al., "An FIR-embedded noise filtering method for $\Delta\Sigma$ fractional-*N* PLL clock generators," *IEEE J. Solid-State Circuits*, vol. 44, no. 9, pp. 2426–2436, Sep. 2009.
- [15] Y. Zhang et al., "A fractional-*N* PLL with space-time averaging for quantization noise reduction," *IEEE J. Solid-State Circuits*, vol. 55, no. 3, pp. 602–614, Mar. 2020.

- [16] B. Razavi, "An alternative analysis of noise folding in fractional- N synthesizers," in *Proc. IEEE Int. Symp. Circuits Syst. (ISCAS)*, Jun. 2018, pp. 1–4.
- [17] L. Kong and B. Razavi, "A 2.4 GHz 4 mW integer- N inductorless RF synthesizer," *IEEE J. Solid-State Circuits*, vol. 51, no. 3, pp. 626–635, Mar. 2016.
- [18] M. H. Perrott, M. D. Trott, and C. G. Sodini, "A modeling approach for Σ - Δ fractional- N frequency synthesizers allowing straightforward noise analysis," *IEEE J. Solid-State Circuits*, vol. 37, no. 8, pp. 1028–1038, Aug. 2002.
- [19] A. Homayoun and B. Razavi, "Analysis of phase noise in phase/frequency detectors," *IEEE Trans. Circuits Syst. I, Reg. Papers*, vol. 60, no. 3, pp. 529–539, Mar. 2013.
- [20] M. Babaie and R. B. Staszewski, "A study of RF oscillator reliability in nanoscale CMOS," in *Proc. Eur. Conf. Circuit Theory Design (ECCTD)*, Sep. 2013, pp. 1–4.
- [21] C. Vaucher et al., "A family of low-power truly modular programmable dividers in standard 0.35- μ m CMOS technology," *IEEE J. Solid-State Circuits*, vol. 35, no. 7, pp. 1039–1045, Jul. 2000.
- [22] Y. Zhao and B. Razavi, "A 19-GHz PLL with 20.3-fs jitter," in *Proc. Symp. VLSI Circuits*, Jun. 2021, pp. 1–2.
- [23] Y. Zhao, O. Memioglu, and B. Razavi, "A 56 GHz 23 mW fractional- N PLL with 110fs jitter," in *IEEE Int. Solid-State Circuits Conf. (ISSCC) Dig. Tech. Papers*, Feb. 2022, pp. 1–3.
- [24] A. Atharav and B. Razavi, "A 56-Gb/s 50-mW NRZ receiver in 28-nm CMOS," *IEEE J. Solid-State Circuits*, vol. 57, no. 1, pp. 54–67, Jan. 2022.
- [25] X. Zhao, Y. Chen, P.-I. Mak, and R. P. Martins, "A 0.0285 mm² 0.68 pJ/bit single-loop full-rate bang-bang CDR without reference and separate frequency detector achieving an 8.2(Gb/s)/ μ s acquisition speed of PAM-4 data in 28 nm CMOS," in *Proc. IEEE Custom Integr. Circuits Conf. (CICC)*, Mar. 2020, pp. 1–4.
- [26] L. Kong, Y. Chang, and B. Razavi, "An inductorless 20-Gb/s CDR with high jitter tolerance," *IEEE J. Solid-State Circuits*, vol. 54, no. 10, pp. 2857–2866, Oct. 2019.
- [27] G. Hou and B. Razavi, "A 56-Gb/s 8-mW PAM4 CDR/DMUX with high jitter tolerance," in *Proc. Symp. VLSI Circuits*, Jun. 2021, pp. 1–2.
- [28] K. M. Megawer et al., "A 5 GHz 370fs_{rms} 6.5 mW clock multiplier using a crystal-oscillator frequency quadrupler in 65 nm CMOS," in *IEEE ISSCC Dig. Tech. Papers*, Feb. 2018, pp. 392–394.



Yu Zhao (Member, IEEE) received the B.S. degree from Shanghai Jiao Tong University, Shanghai, China, in 2013, and the M.S. and Ph.D. degrees in electrical engineering from the University of California at Los Angeles, Los Angeles, CA, USA, in 2015 and 2022, respectively.

From 2015 to 2018, he was with Ubilinx Technology, Inc., San Jose, CA, USA, where he was worked on frequency synthesizers for Bluetooth and WiFi 6. He is currently with the RFIC Design Team, Hisilicon, Shanghai. His research interests include

low-jitter frequency synthesizers for wireless and wireline transceivers.



Onur Memioglu (Member, IEEE) received the B.Sc. and M.Sc. degrees in electrical and electronics engineering from Middle East Technical University, Ankara, Turkey, in 2015 and 2018, respectively, and the Ph.D. degree from the Communication Circuits Laboratory, University of California at Los Angeles, Los Angeles, CA, USA, in 2021.

He was an RFIC Design Engineer with Mikro-Tasarim, Ankara, from 2015 to 2018. He is currently with the RFIC Design Team, Apple, Cupertino, CA, USA.



Long Kong (Member, IEEE) received the B.E. degree in microelectronics from Shanghai Jiao Tong University, Shanghai, China, in 2011, and the M.S. and Ph.D. degrees in electrical engineering from the University of California at Los Angeles, Los Angeles, CA, USA, in 2013 and 2016, respectively.

In 2016, he joined Oracle, Santa Clara, CA, USA, as a Senior Hardware Engineer, where he was working in high-speed SerDes transceivers. He then joined Apple Inc., Cupertino, CA, USA, in 2017, as an RFIC Design Engineer. He has been working in Bluetooth and ultra-wideband radios for wearable and mobile devices. His research interests include frequency synthesizers, wireless and wireline transceivers, radars, and clock recovery for data communication systems.

Dr. Kong was a recipient of the Qualcomm Innovation Fellowship from 2013 to 2014, the Analog Devices Outstanding Student Designer Award in 2015, and the Broadcom Fellowship from 2015 to 2016.



Behzad Razavi (Fellow, IEEE) received the B.S. degree from the Sharif University of Technology, Tehran, Iran, in 1985, and the M.S. and Ph.D. degrees from Stanford University, Stanford, CA, USA, in 1988 and 1992, respectively, all in electrical engineering.

He was an Adjunct Professor with Princeton University, Princeton, NJ, USA, from 1992 to 1994, and with Stanford University in 1995. He was with AT&T Bell Laboratories and Hewlett-Packard Laboratories until 1996. Since 1996, he has been an

Associate Professor and subsequently a Professor of electrical engineering with the University of California at Los Angeles, Los Angeles, CA, USA. He has authored *Principles of Data Conversion System Design* (IEEE Press, 1995), *RF Microelectronics* (Prentice Hall, 1998, 2012) (translated to Chinese, Japanese, and Korean), *Design of Analog CMOS Integrated Circuits* (McGraw-Hill, 2001, 2016) (translated to Chinese, Japanese, and Korean), *Design of Integrated Circuits for Optical Communications* (McGraw-Hill, 2003, Wiley, 2012), *Design of CMOS Phase-Locked Loops* (Cambridge University Press, 2020), and *Fundamentals of Microelectronics* (Wiley, 2006, 2014, 2021) (translated to Korean, Portuguese, and Turkish), and is the Editor of *Monolithic Phase-Locked Loops and Clock Recovery Circuits* (IEEE Press, 1996) and *Phase-Locking in High-Performance Systems* (IEEE Press, 2003). His research interests include wireless and wireline transceivers and data converters.

Dr. Razavi is a member of the U.S. National Academy of Engineering and a fellow of the U.S. National Academy of Inventors. He received the Beatrice Winner Award for Editorial Excellence at the 1994 ISSCC, the Best Paper Award at the 1994 European Solid-State Circuits Conference, the Best Panel Award at the 1995 and 1997 ISSCC, the TRW Innovative Teaching Award in 1997, the Best Paper Award at the IEEE Custom Integrated Circuits Conference in 1998, and the McGraw-Hill First Edition of the Year Award in 2001. He was the co-recipient of both the Jack Kilby Outstanding Student Paper Award and the Beatrice Winner Award for Editorial Excellence at the 2001 ISSCC. He received the Lockheed Martin Excellence in Teaching Award in 2006, the UCLA Faculty Senate Teaching Award in 2007, and the CICC Best Invited Paper Award in 2009 and 2012. He was a co-recipient of the 2012 and 2015 VLSI Circuits Symposium Best Student Paper Awards and the 2013 CICC Best Paper Award. He was also recognized as one of the top ten authors in the 50-year history of ISSCC. He received the 2012 Donald Pederson Award in Solid-State Circuits. He was also a recipient of the American Society for Engineering Education PSW Teaching Award in 2014 and the 2017 IEEE CAS John Choma Education Award. He has served as an IEEE Distinguished Lecturer. He served on the Technical Program Committees of the International Solid-State Circuits Conference (ISSCC) from 1993 to 2002 and the VLSI Circuits Symposium from 1998 to 2002. He has also served as a Guest Editor and an Associate Editor for the IEEE JOURNAL OF SOLID-STATE CIRCUITS, IEEE TRANSACTIONS ON CIRCUITS AND SYSTEMS, and *International Journal of High Speed Electronics*. He served as the Founding Editor-in-Chief for the IEEE SOLID-STATE CIRCUITS LETTERS.